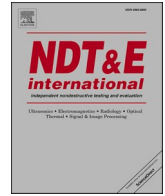| Title	Experimental investigation of defect imaging using a phased array probe with a stacked plate buffer
Author(s)	Xia, Mingqian; Hayashi, Takahiro; Mori, Naoki
Citation	NDT and E International. 2025, 151, p. 103316
Version Type	VoR
URL	https://hdl.handle.net/11094/100389
rights	This article is licensed under a Creative Commons Attribution-NonCommercial 4.0 International License.
Note	

Experimental investigation of defect imaging using a phased array probe with a stacked plate buffer

Mingqian Xia , Takahiro Hayashi [*] , Naoki Mori

Department of Mechanical Engineering, Graduate School of Engineering, Osaka University, Suita, Osaka, 565-0871, Japan

ARTICLE INFO

ABSTRACT

The authors have previously validated defect imaging using stacked plate buffer and a phased array probe by numerical simulations. This study experimentally verifies the feasibility of this approach. A stacked plate buffer created by considering the dispersion of the S0 mode of Lamb waves was used for the first experiments, which showed that high intensity spurious areas appeared and defect images were blurred. Numerical analysis of the propagation of S0 modes in the plate revealed that trailing waves cause the high intensity spurious areas. Theoretical and numerical analyses indicated that the trailing waves can be removed by increasing the width of the plate. Finally, experiments using wider plates verified that a phased array probe with a stacked plate buffer can eliminate the high intensity spurious areas and clarify the defect images.

1. Introduction

All plants, including nuclear and thermal power plants, steel plants, and chemical plants, require regular inspections to ensure their safe operation. These inspections range from visual inspections during plant operation to ultrasonic and radiological inspections during plant downtime, and cover a wide variety of components such as pipework, tanks and electrical equipment. In particular, a large number of pipes are stretched throughout the plant, and stress corrosion cracking (SCC) and fatigue cracking can occur in pipes depending on the type of content and changes in pressure [1–7].

The heat-affected zones (HAZs) near welds in pipes are often the starting point of pipe collapse due to SCC and fatigue cracks. In the inspection of HAZs in nuclear power plants, for example, ultrasonic inspection is used to precisely locate the crack tip position to assess the remaining service life in consideration of the operating environment [8–18].

Ultrasonic Phased Array (PA) technique has become widely used in the field of NDT such as crack sizing in HAZs, in which many piezoelectric elements arranged at equal intervals emit and receive ultrasonic signals and the ultrasonic signals are converted into a defect image by an imaging algorithm. Commonly used data acquisition and imaging techniques are Plane Wave Imaging (PWI) and Full Matrix Capture/ Total Focusing Method (FMC/TFM). The former method incidents ultrasonic waves into a tested material from N elements at once, where the

number of elements is assumed to be N, and processes N signals received at N elements. In the latter method, $N \times N$ signals are collected by switching the incident element and receiving with N elements, and a defect image is created from the $N \times N$ signals [19–24].

Although the ultrasonic PA imaging is becoming a standard method for defect imaging of solid materials, it may be problematic when considering its use for monitoring high temperature in-service piping. For example, the use of liquid sodium as a coolant is being considered for new nuclear power plant, where the pipelines for transporting the coolant are often working in high temperature around 500 °C. To maintain the function of a PA transducer, the working temperature of the probe should be kept up to 60 °C.

A buffer rod can be a solution for ultrasonic testing in high temperature. Other than transmitting the ultrasonic waves, the buffer rod can also keep the contact region with the ultrasonic probe in a tolerable temperature range by being cooled with coolant such as water and air. Although a buffer rod can be used for single ultrasonic probe in ultrasonic pulse echo technique, it has never been used for the PA imaging. This is because images cannot be obtained due to the diffraction limit, where beam forming by a PA probe cannot be achieved using a buffer rod [25–27].

In our previous papers, a stacked plate structure was considered to instead of a bulk buffer rod as a solution for the PA imaging with a buffer. Fukuchi. et al. numerically investigated the ultrasonic focusing by a stacked plate structure and showed that ultrasonic focusing is

possible by stacked thin plate structure beyond the diffraction limit [28]. Based on the numerical analyses of the wave propagation in the stacked plate structure, the next paper showed numerically that the defect imaging with a PA probe with a stacked plate buffer is possible but is limited due to the multiple reflections from the buffer ends [29].

The purpose of this research is to confirm the feasibility of the PA imaging with a stacked plate buffer experimentally. In Section 2, the principle of the PA imaging with a stacked plate buffer is explained. Section 3 describes the experimental conditions, including the information of PA probe, specimen, buffer and the imaging algorithms used in the experiment. The results of the first experiment are also provided in this section. In Section 4, the cause of the spurious images obtained in the first experiments are investigated both theoretically and numerically. Based on the analyses, defect imaging is improved in Section 5.

2. Phased array imaging with a stacked-plate buffer

Our previous work proved by numerical simulations that PA technology such as beam focusing and defect imaging can be used within the solid material when a stacked-plate buffer is attached to a PA probe, as shown in Fig. 1 [29]. In this section, the principle of the PA imaging with a stacked plate buffer is briefly explained using Lamb wave dispersion curves.

A stacked plate buffer consists of a series of thin flat plates, the pitch and thickness of which are adjusted so that each piezoelectric element of the PA probe corresponds to an end of single thin plate. When the PA probe is brought into contact with the end of the stacked-plate buffer, the vibrations of the individual piezo elements propagate directly through the plate to the opposite end. In other words, even in the presence of a buffer, the object in contact with the buffer can be vibrated, just as if the PA probe were in direct contact with the object. This makes use of the nature of the S0 mode of Lamb wave propagating through the thin plate.

The individual vibrating elements of the PA probe emit longitudinal waves with displacements perpendicular to the vibrating surface, so that vibrations in the longitudinal dir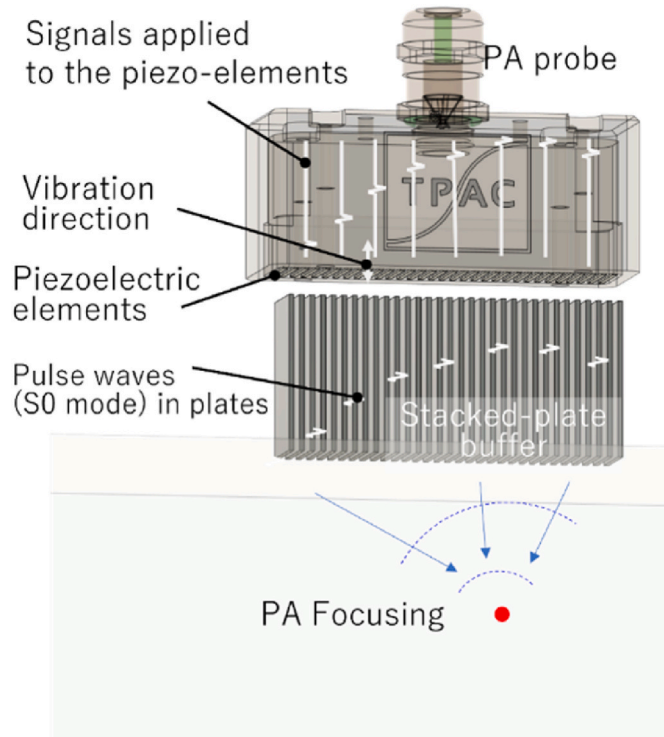ection of the thin plate are incident on the edge surface of the thin plate. Because this vibration resembles the vibration distribution of the S0 mode in the cross-section of the thin plate, most of the Lamb modes propagating in the thin plate are the S0 mode. Fig. 2 shows the group velocity dispersion curve of Lamb waves for a stainless-steel plate of thickness d with longitudinal and transverse wave velocities of $c_L = 5790$ m/s and $c_T = 3100$ m/s, respectively, where the horizontal axis is represented by the product of frequency f and plate thickness d and the vertical axis by the group velocity. The S0 mode is less dispersive in the low fd region and approaches plate velocity ($c_{plate} = 2c_T\sqrt{1 - (c_T/c_L)^2} = 5236$ m/s) at $fd \to 0$. Considering the S0 mode in the low fd range, the propagating pulse wave reaches the opposite end of the plate with a small change in shape. When these ends are in contact with the object and delays are given to the elements in the PA probe as shown in Fig. 1, for example, the delays given are maintained and the ultrasonic pulses propagate almost unchanged. Resultingly ultrasonic focusing can be achieved in the object as shown in Fig. 1. Other than the focusing, numerical calculations have shown that PWI and TFM/FMC can also be used to image defects even with a stacked plate buffer [29]. In other words, it is expected that ultrasonic PA technology can be used almost without modification by using a thin plate buffer.

3. Defect imaging experiments using a PA probe attached with a stacked-plate buffer

This section describes the experimental set-up and test specimen for the imaging experiment using a PA probe with the proposed stacked plate buffer, and then presents the first results of the imaging experiment on a test specimen with artificial defects.

A linear array PA probe consisting of 64 elements with an element size of 15 mm × 0.9 mm, a pitch of 1 mm, an element gap of 0.1 mm, and a total aperture of 15 mm × 63.9 mm, is used to collect the experimental data by PWI and FMC. All elements exhibit nearly identical bandwidths with a center frequency of 1.0 MHz and a full width at half maximum of about 1.0 MHz. The array was driven by PA equipment (The Phased Array Company, Explorer). The system uses a 14 bit and 64-channel architecture and can perform the acquisition of all the 64 channels in parallel at a sampling frequency of 50 MHz. In these experiments, the controller was driven from a PC using the LabVIEW interface. Each element of the PA probe can apply longitudinal force on the edge of each
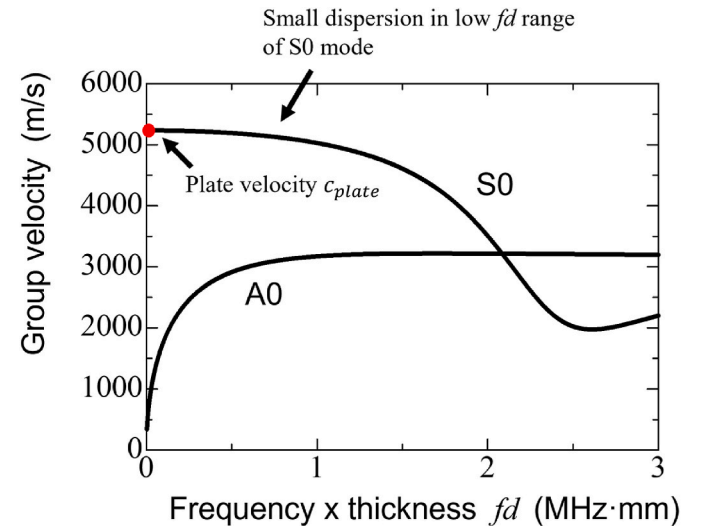

Fig. 1. Schematic diagram of phased array focusing with a stacked-plate buffer.

Fig. 2. Group velocity dispersion curves of Lamb wave in the low fd range for the plate with longitudinal and transverse wave velocities of 5790 m/s and 3100 m/s, respectively, and the velocity of S0 mode at $fd = 0$, called plate velocity, is 5236 m/s.

buffer plate and incident an ultrasonic pulse wave with the center frequency of 1 MHz into each buffer plate which each piezoelectric element paired with.

Fig. 3 shows a picture of the stacked plate buffer and a single stainless-steel (SUS304) plate used in the experiments in this section. The SUS304 plate is 0.9 mm thick, the same thickness as the piezo element of the PA probe, and 100 mm long, the same length of the buffer used in the previous numerical verification. The width of the buffer was 50 mm. 64 plates were assembled using a double-sided tape with a nominal thickness of 0.09 mm, which is the closest to 0.1 mm, the gap between the piezoelectric elements of the PA probe, among commercially available double-sided tapes. The gap between the elements of the PA probe and the thickness of the tape was slightly different, but the aperture did not have a large error after assembly. The double-sided tape was 5 mm wide and was applied to the upper side where the PA transducer contacts and the bottom side where the object to be inspected contacts, as shown in the figure. In addition to the purpose of attaching the plates, the tape was also used to prevent the couplant applied to the upper and lower edges from penetrating between the thin plates. The area where the double-sided tape is attached to the plate was small to minimize crosstalk, which is the propagation of waves through the double-sided tape to the plate next to it. Since a longitudinal wave with a center frequency of 1 MHz was incident on the upper surface of the plate, S0 mode of Lamb waves, which has a similar vibration form to the longitudinal wave, propagates significantly in the thin plate. Considering that the plate thickness is 0.9 mm, and $fd = 0.9$ MHz-mm, the S0 mode propagates in the small dispersion range as shown in Fig. 2 [29].

As shown in Fig. 4, the aluminum alloy (A5052) specimen is a 100 mm × 100 mm × 50 mm rectangular solid having three side drilled holes (SDH). The SDHs #1, #2, and #3 located 20 mm, 25 mm, and 30 mm from the upper surface, and 20 mm, 40 mm, and 60 mm from the left surface, respectively. The diameter of # 1 and #3 are 3.0 mm, while that of #2 is 3.5 mm.

Waveforms were collected and processed in two-different ways, PWI and FMC/TFM, for defect imaging. Assuming that a PA probe with N elements, for PWI, all piezo elements excite the signals simultaneously and all the elements collect waveforms. As a result, $1 \times N$ waveforms are collected in one measurement. For FMC/TFM, in each testing period, one element emits the signal and all the elements receive the echo from the specimen. Repeating such pulse emission from a single element and
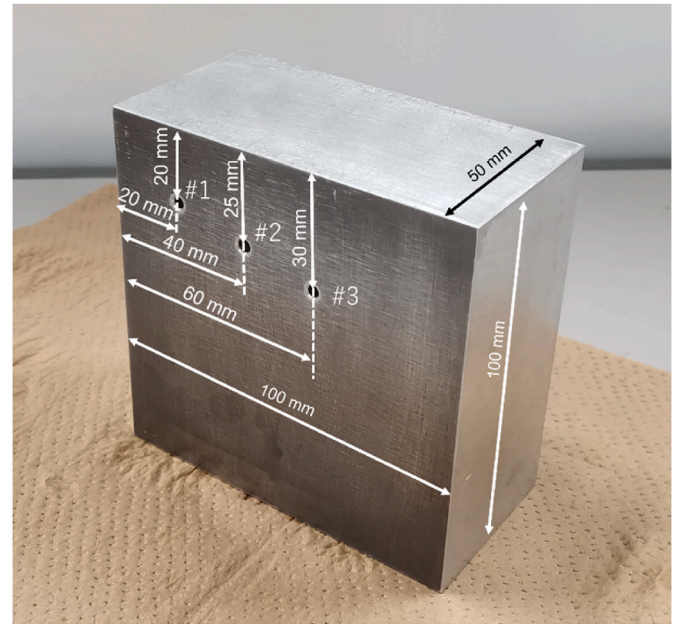

Fig. 4. A picture of the specimen with three side-drilled holes as internal reflectors to test the effectiveness of the stacked plate buffer.

signal acquisition with all elements collect $N \times N$ waveforms. Then the delay and sum processing based on the TFM are applied to all the waveforms. Expected delay is used to calculate the intensity of each specific position in the imaging area [21].

Before imaging experiments with a stacked plate buffer, imaging experiments were done by the PA probe without the buffer as shown in Fig. 5 (a). After confirming defect images can be obtained with the PA probe, imaging experiments with a stacked plate buffer were done as shown in Fig. 5 (b). In all experiments, a regular couplant for longitudinal waves was applied between the PA probe and specimen, PA probe and buffer, and buffer and specimen. In actual inspections at high temperatures, it is necessary to use adhesives or couplant that can be used at the high temperatures expected. The imaging areas, called
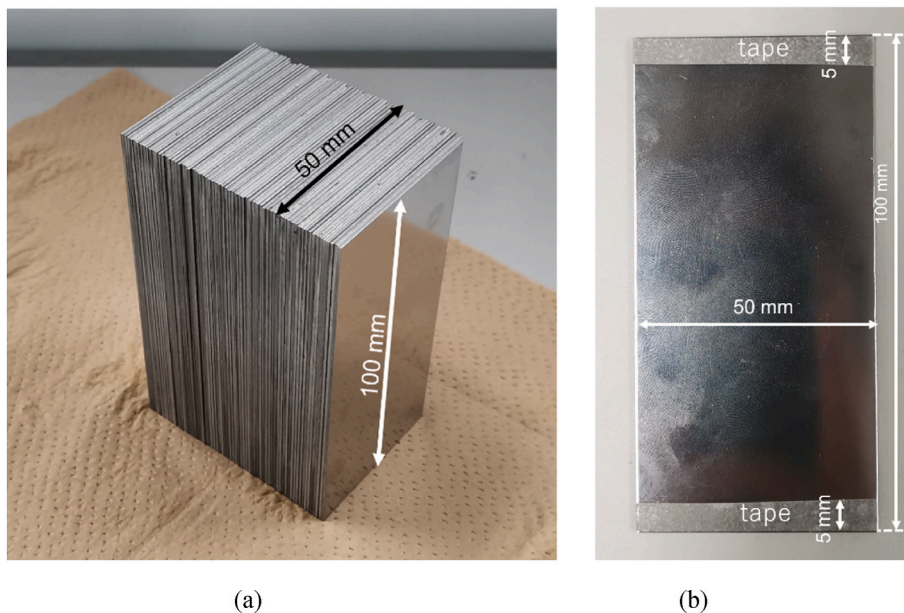

(a)

(b)

Fig. 3. Pictures of (a) a stacked plate buffer hat has been formed by buffer plates, and (b) a single buffer plate attached by tapes before attached with other buffer plate.
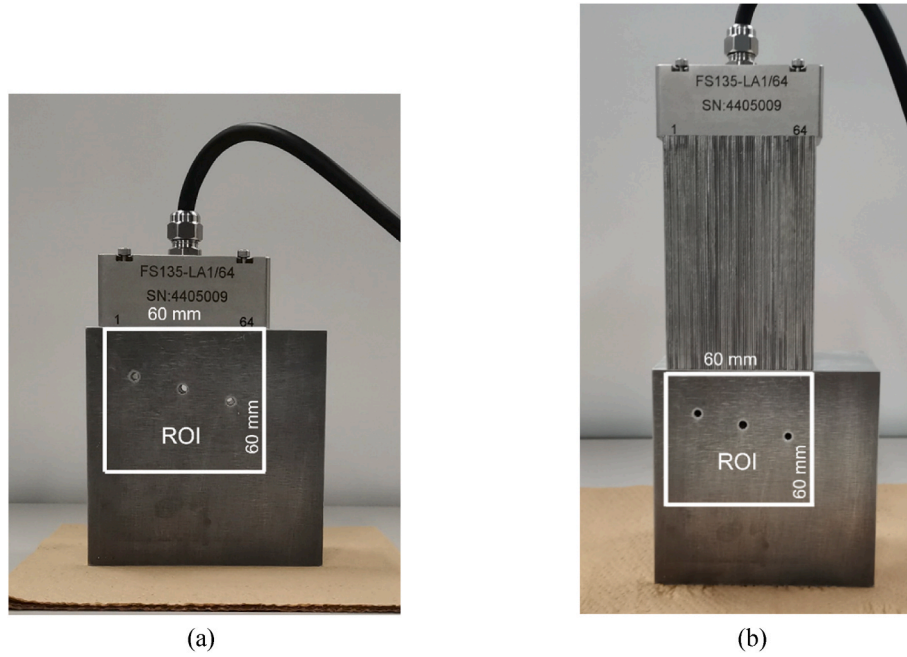
Fig. 5. Pictures of the experimental devices and specimen when (a) phased array probe without a stacked plate buffer, and (b) with the stacked plate buffer.

regions of interest (ROI), were the squares of 60 mm × 60 mm shown in the figures. The upper and lower edges of the stacked plate buffer were attached to the PA probe and the upper surface of the specimen, respectively. A coupling medium for longitudinal wave probes was applied to these contact surfaces.

Fig. 6 shows the defect images in the first experiments using the PA probe with and without the buffer shown in Fig. 3. Defect images were obtained using the PWI and FMC/TFM without buffer as shown in Fig. 6 (a) and (b), respectively. Then, the defect images were obtained using the PA probe with the buffer as shown in Fig. 6(c) and (d). These imaging processes were performed assuming that the S0 mode with a phase velocity of 5100 m/s propagate in the buffer and longitudinal waves with a velocity of 6400 m/s propagate in the aluminum specimen. The colors of the images represent intensities calculated by the PWI or TFM, normalized by the maximum intensity of each figure.

In (a) and (b) without a buffer, clear SDH images were obtained at the appropriate positions. However, in (c) and (d) using the buffer, the SDH images were blurred because high intensity areas appear around 40 mm from the top. The reason for this high intensity areas is discussed in the next section using numerical calculations.

4. Numerical analysis to investigate the cause of spurious images

To investigate the cause of the high intensity areas, numerical calculations of wave propagation in a thin plate were carried out in this section. Considering the plate is thin, two-dimensional calculations were done under the plane stress condition by COMSOL Multiphysics®. Although this assumption may not adequately represent the dispersion of Lamb waves, it was sufficient to identify the cause of the problem here, saving significant computation time and memory. Firstly, the wave propagation in a 100 mm × 50 mm plate was investigated. Two-dimensional plane stress calculation was performed by applying the vertical dynamic normal force to the width of 15 mm at the upper end of the plate with a center frequency of 1 MHz to simulate the dynamic force from the PA probe used in the experiments. All boundaries around the rectangular thin plate were assumed to be traction free boundaries. Fig. 7 shows the snapshots of the propagating waves at four different time steps: (a) 9 μs just after the dynamic normal force is applied at the

upper end, (b) 19 μs when the incident wave arrives at the lower end of the plate, (c) 39 μs when the main straight wave packet reaches the upper end of the plate, (d) 52 μs when a trailing wave reaches the upper end of the plate. As shown in Fig. 7 (a), the incident wave from the top of the plate spreads as it propagates. Then the spreading incident wave reflects and generates mode converted shear horizontal (SH) waves at both side edges, and the mode converted SH waves appear as oblique lines from both side edges behind the main straight propagating wave packet, as shown in Fig. 7 (b). At the end of the oblique lines, the horizontally straight wave can be seen, as shown in (c). This is known as a trailing pulse [30], which appears with the interval from the main straight wave described as the following equation.

$$\Delta t = \frac{w}{c_T \cos\alpha} - \frac{w}{c_{plate}}\tan\alpha \tag{1}$$

where w, c_T, c_{plate} are the width of the plate, transverse wave velocity (SH wave velocity), a plate wave velocity, respectively, and α is the $\sin^{-1}\left(c_T/c_{plate}\right)$. In the case of the bulk wave propagation in a plate with the thickness of w and the infinite width, longitudinal wave velocity c_L should be used instead of c_{plate} [30]. In Fig. 7 (c), this trailing wave arrives at the upper end approximately 13 ms after the first main straight wave packet, which agrees well with Eq. (1). This travelling time corresponds to a propagation distance of about 80 mm inside the test specimen, which indicates the cause of the high intensity areas in Fig. 6 (c) and (d) is the trailing wave that behaved as if the reflectors were located 40 mm from the upper surface of the test specimen.

To solve the problem of high intensity areas caused by the trailing wave shown in Fig. 7, buffer plates with different widths were used to investigate the relation between the width of the buffer plate and the travelling time of the trailing wave. Two-dimensional plane stress calculations were performed under the same conditions as in Fig. 7, except the width of the plates. Calculations were carried out for 30 mm, 70 mm, and 100 mm wide plates. Fig. 8 shows the snapshots of the wave propagation in three buffer plates with different widths at the time step when the main straight wave packet reaches the upper end of the plate. As shown in Fig. 8 (a) for a 30 mm wide plate, the trailing wave arrives at the upper end about 8 ms after the first main straight wave, which corresponds to a propagation distance of about 50 mm inside the test specimen and can produce a high intensity area located about at 25 mm
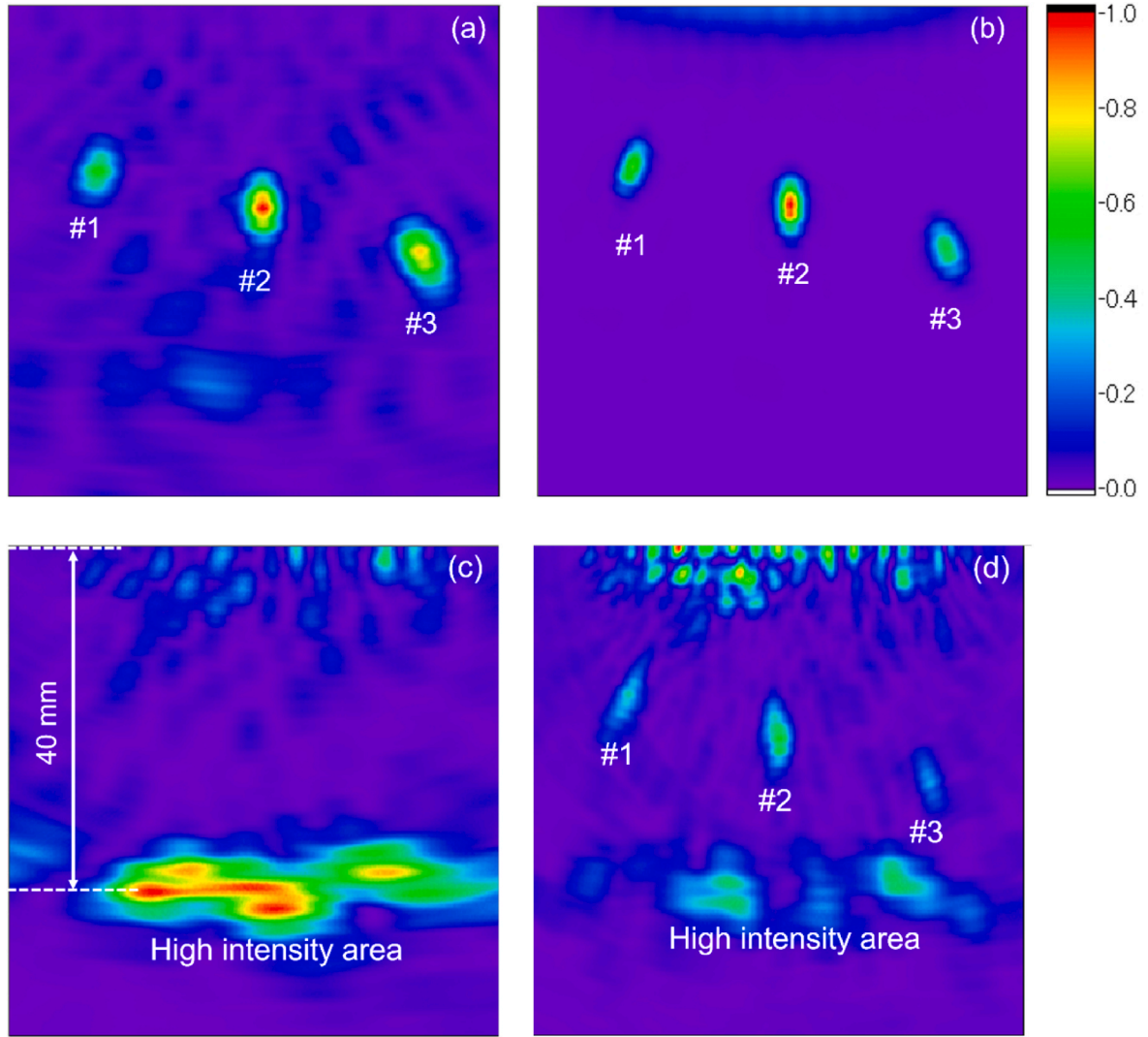
Fig. 6. Defect images when using the PA probe with and without the stacked plate buffer. (a) PWI and without buffer. (b) FMC/TFM without buffer. (c) PWI with buffer. (d) FMC/TFM with buffer.

from the upper surface of the test specimen. As shown in Fig. 8(b) and (c), for 70 mm and 100 mm wide plates, respectively, the trailing waves were not observed in the snapshots when the main wave straight packet reaches the upper end of the plate. In this condition, the time of the trailing wave arrives at the upper end of the buffer plate will be more than 18 ms after the main straight wave packet. Comparing the snapshots shown in Figs. 7 (c) and Fig. 8, we can draw the conclusion that the time gap between the main wave packet of the reflected wave and the trailing wave becomes larger by expanding the width of the buffer plate, where the high intensity area shown in Fig. 6 (c) and (d) can be farther away from the ROIs.

5. Experiments using stacked plate buffers with different widths

To test the performances of the stacked plate buffers consisting of 30 mm, 70 mm, and 100 mm wide plates, imaging experiments were conducted. All the buffer plates have 100 mm long and 0.9 mm thick. The preparation of the stacked plate buffers and the experimental process are the same as done in 50 mm width buffer, described in Section 2. The same specimen was used in the experiments.

Fig. 9 shows the imaging results: (a) and (b) for 30 mm wide plate, (c) and (d) for 70 mm wide plate, and (e) and (f) for 100 mm wide plate, respectively, and (a), (c), (e) were created by PWI, and (b), (d), (f) were

created by FMC/TFM, respectively. For 30 mm wide plate in Fig. 9(a) and (b), high intensity areas are shown in the ROIs around 25 mm and 50 mm from the top. Defect images cannot be observed due to the high intensity areas. The high intensity areas around 25 mm from the top were created by the trailing wave as described in the previous section, that is, $\Delta t = 8$ μs for a 30 mm wide plate and this corresponds to the roundtrip distance of 25 mm in the test specimen. Because the trailing waves appears repeatedly at intervals of Δt [30], the high intensity areas around 50 mm from the top were created by the second trailing wave.

Comparing (a) and (b), it can be seen that the high intensity area in (a) of PWI is wider and greater than that in (b) of FMC/TFM. This is due to the difference in signal processing between PWI and FMC/TFM. In PWI, pulse waves are incident simultaneously from all piezoelectric elements and received by all of them, where all of the received signals include the trailing waves reflected from the buffer plate end, and the signals including these trailing waves are processed to obtain an image of the inside of the test specimen. On the other hand, FMC/TFM repeats the measurements in which the incident wave outputs from one piezoelectric element and all piezoelectric elements receive the reflected waves. When the incident element and the receiving element are the same, the received signal contains trailing waves in the buffer plate, but the other received signals, in which the incident and receiving elements are different, contain very small trailing waves that have come around
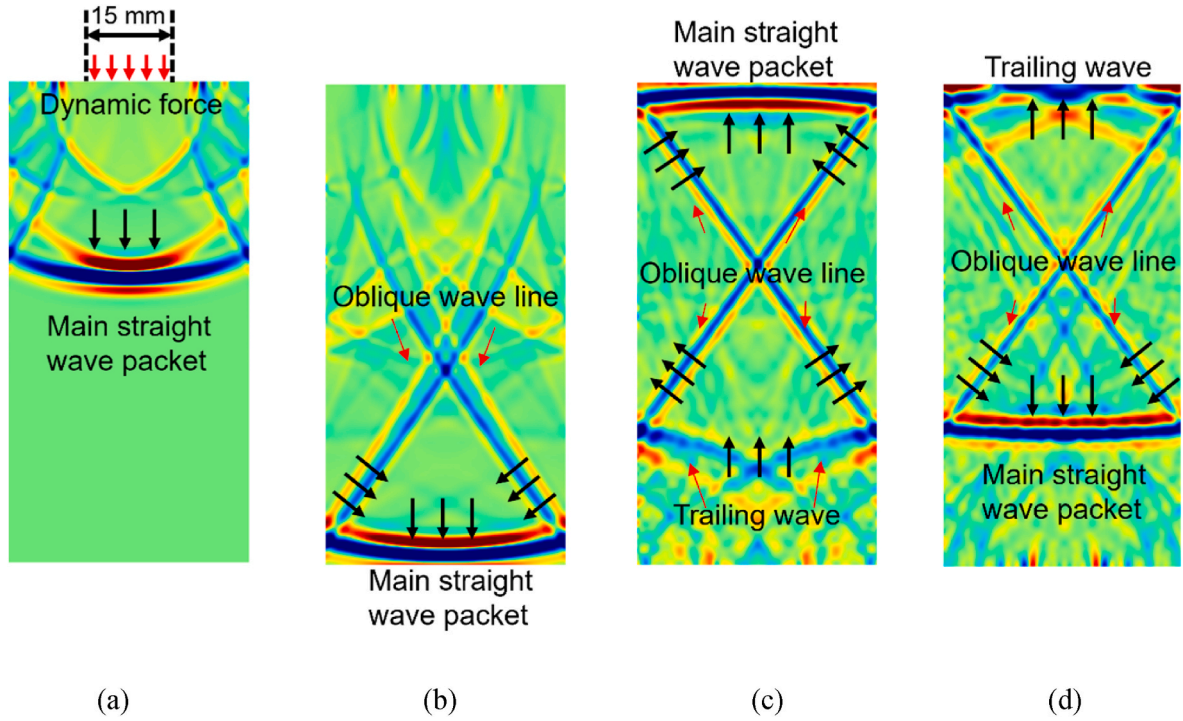
Fig. 7. Snapshots of wave propagation in a plate with 100 mm × 50 mm plate at (a) 9 μs after the dynamic normal force is applied at the upper end, (b) 19 μs when the incident wave arrives at the lower end of the plate, (c) 39 μs when the main straight wave packet reaches the upper end of the plate, (d) 52 μs when a trailing wave reaches the upper end of the plate. The color represents the displacement in the vertical direction. The black arrow represents the direction of the wave propagation. (For interpretation of the references to color in this figure legend, the reader is referred to the Web version of this article.)
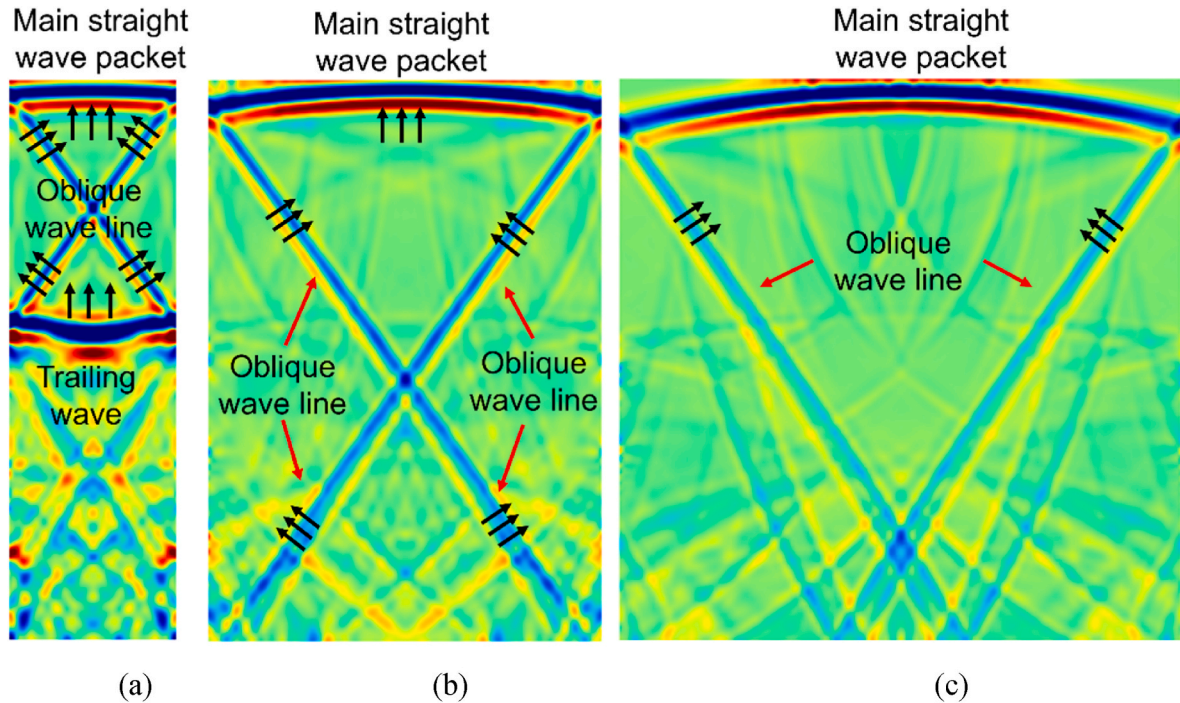

Fig. 8. Snapshots of the wave propagation for (a) 30 mm, (b) 70 mm and (c) 100 mm wide plates. All the snapshots show the waveforms at 39 μs when the main straight wave packet reaches the upper end of the plate.

through the test specimen. The influence of trailing waves is reduced in FMC/TFM because these received waveforms are processed and imaged.

When the width of the buffer plates expanded to be 70 mm, shown in Fig. 9(c) and (d), the images of the SDHs are clearer compared with the imaging results for 50 mm wide plate shown in Fig. 6(c) and (d). Only

small horizontal area can be seen at the bottom of the ROIs, due to the trailing wave. In this condition, the influence from the trailing wave to the imaging result decreases compared with results for narrower plates.

For 100 mm wide plate, as shown in Fig. 9(e) and (f), the high intensity areas caused by the trailing wave are totally removed from the
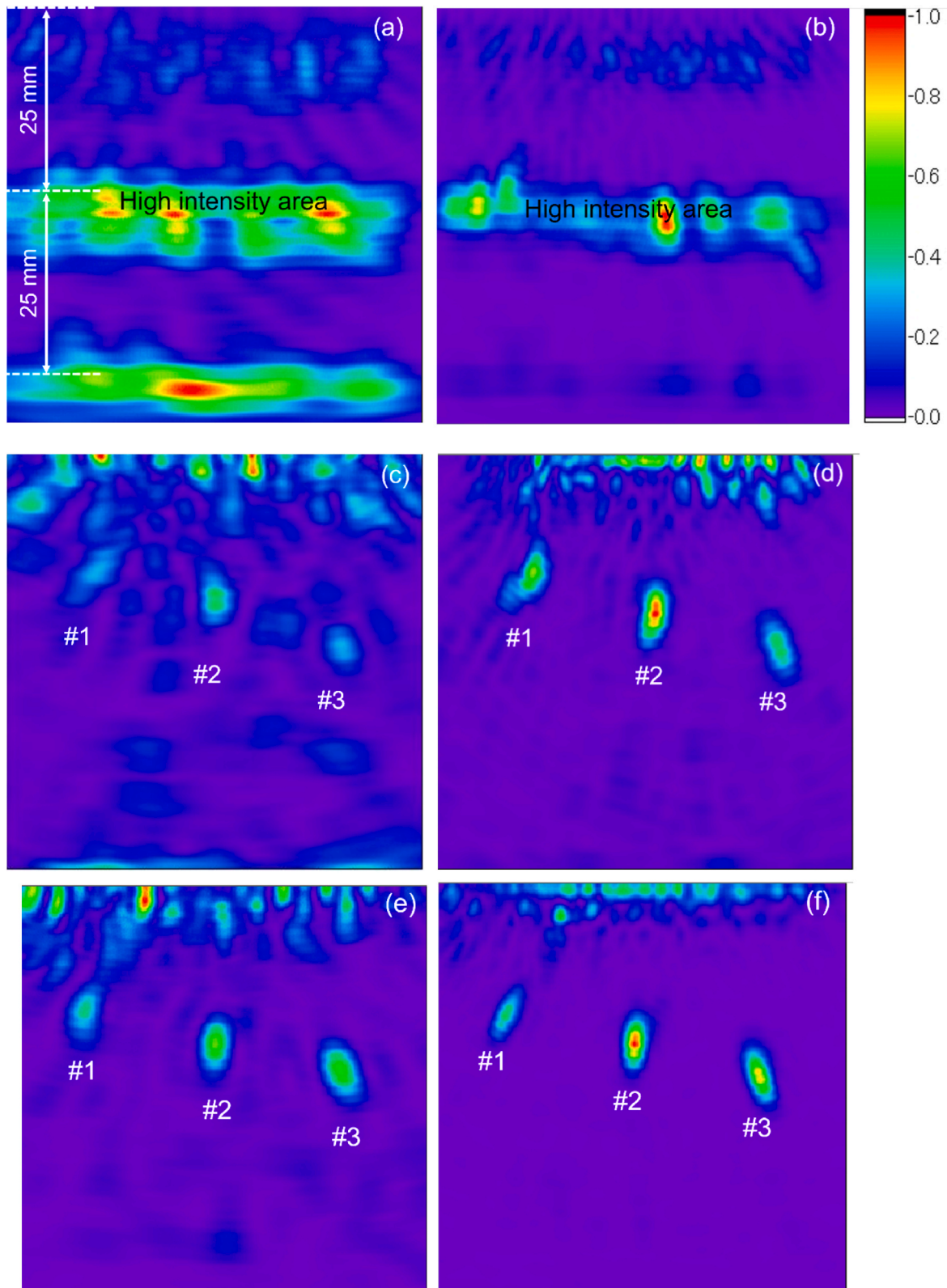
Fig. 9. Defect images using the PA probe with the stacked plate buffer with different widths and different imaging processes. (a) 30 mm wide buffer and PWI. (b) 30 mm wide buffer and FMC/TFM. (c) 70 mm wide buffer and PWI. (d) 70 mm wide buffer and FMC/TFM. (e) 100 mm wide buffer and PWI. (f) 100 mm wide buffer and FMC/TFM.

ROIs. and therefore, images of the SDHs are clearer than those using narrower plates.

Summarizing the experimental results in Fig. 9, the high intensity spurious areas caused by the trailing waves in the stacked plate buffer can be removed using wider buffer plates.

6. Conclusion

The feasibility of defect imaging using a PA probe attached with a stacked plate buffer was experimentally investigated. SDHs in an aluminum specimen were imaged using a linear array probe with 64 elements at a center frequency of 1 MHz and a stacked plate buffer consisting of a 0.9 mm thick, 100 mm long SUS plate. In the case of the buffer with a 50 mm wide plate, large spurious images appeared in the defect image. Numerical simulations proved that this was caused by trailing waves originating from SH waves due to mode conversion at the both sides of the plate, and the results agreed well with previous theoretical studies. In order to reduce the influence of the trailing waves on defect images, a wider plate was used, and a very clear defect image was obtained. The imaging technique using a PA probe with the stacked plate buffer is expected to be used to inspect high-temperature objects.

CRediT authorship contribution statement

Mingqian Xia: Writing – review & editing, Writing – original draft, Validation, Software, Methodology, Investigation, Formal analysis. **Takahiro Hayashi:** Writing – review & editing, Writing – original draft, Validation, Supervision, Software, Project administration, Methodology, Investigation, Data curation, Conceptualization. **Naoki Mori:** Writing – review & editing, Validation, Supervision, Project administration, Funding acquisition, Formal analysis, Conceptualization.

Declaration of competing interest

The authors declare the following financial interests/personal relationships which may be considered as potential competing interests: Takahiro Hayashi reports financial support, administrative support, equipment, drugs, or supplies, and travel were provided by Japan Society for the Promotion of Science. Takahiro Hayashi reports a relationship with Osaka University that includes: employment and travel reimbursement. If there are other authors, they declare that they have no known competing financial interests or personal relationships that could have appeared to influence the work reported in this paper.

Acknowledgements

Data availability

Data will be made available on request.

References

[1] Sposito G, Ward C, Cawley C, Nagy PB, Scruby C. A review of non-destructive techniques for the detection of creep damage in power plant steels. NDT E Int 2010; 43(7):555–67. https://doi.org/10.1016/j.ndteint.2010.05.012.

[2] Morgan BC, Tilley R. Inspection of power plant headers utilizing acoustic emission monitoring. NDT E Int 1999;32(3):167–75. https://doi.org/10.1016/S0963-8695 (98)00068-1.

[3] Ma J, Jiang J. Applications of fault detection and diagnosis methods in nuclear power plants: a review. Prog Nucl Energy 2011;53(3):255–66. https://doi.org/ 10.1016/j.pnucene.2010.12.001.

[4] Alleyne DN, Pavlakovic B, Lowe MJS, Cawley P. Rapid, long range inspection of chemical plant pipework using guided waves. AIP Conf Proc 2001;557:180–7. https://doi.org/10.1063/1.1373757.

[5] Oh S, Yun DS, Kim J. Evaluation of high-temperature degradation of platen superheater tube in thermoelectric power plant using nonlinear surface ultrasonic waves. Ultrasonics 2024;136:107162. https://doi.org/10.1016/j. ultras.2023.107162.

[6] Shin IH, Park SK, Kim SY, Seok CS, Koo JM. Effect of welding parameters on fracture resistance characteristics of nuclear piping. Int J Precis Eng Manuf 2015; 16:65–71. https://doi.org/10.1007/s12541-015-0008-2.

[7] Pu W, Raman AAA, Hamid MD, Gao X, Lin S, Buthiyappan A. Process & occupational safety integrated inherently safer chemical plant design: framework development and validation. J Loss Prev Process Ind 2024;87:105204. https://doi. org/10.1016/j.jlp.2023.105204.

[8] Fan E, Li Y, Lv X. A study on the stress corrosion mechanism of microstructures in a heat-affected zone of high-strength steel weldment in artificial seawater. Surf Topogr Metrol Prop 2021;9:025040.

[9] Takaya S, Miya K. Application of magnetic phenomena to analysis of stress corrosion cracking in welded part of stainless steel. J Manuf Process 2005;161: 66–74. https://doi.org/10.1016/j.jmatprotec.2004.07.017.

[10] Sugawara A, Jinno K, Ohara Y, Yamanaka K. Closed-crack imaging and scattering behavior analysis using confocal subharmonic phased array. Jpn J Appl Phys 2015; 54:07HC08. https://doi.org/10.7567/JJAP.54.07HC08.

[11] Yu L, Liu Y, Deng H, Zhang S, Wang Y, Zhou Y. Cracking failure analysis of pipe to flange weld joint. IOP Conf Ser Earth Environ Sci 2021;859:012012. https://doi. org/10.1088/1755-1315/859/1/012012.

[12] Vasilev M, MacLeod C, Galbraith W, Javadi Y, Foster E, Dobie G, Pierce G, Gachagan A. Non-contact in-process ultrasonic screening of thin fusion welded joints. J Manuf Process 2021;64:445–54. https://doi.org/10.1016/j. jmapro.2021.01.033.

[13] Khodamorad SH, Alinezhad N, Haghshenas Fatmehsari D, Ghahtan K. Stress corrosion cracking in Type.316 plates of a heat exchanger. Case Stud Eng Fail Anal 2016;5–6:59–66. https://doi.org/10.1016/j.csefa.2016.03.001.

[14] Suleimanov RI, Zainagalina LZ, Khabibullin MY, Zaripova LM, Kovalev NO. Studying heat-affected zone deformations of electric arc welding. IOP Conf Ser Mater Sci Eng 2018;327:032053. https://doi.org/10.1088/1757-899X/327/3/ 032053.

[15] Ohara Y, Yamamoto S, Mihara T, Yamanaka K. Ultrasonic evaluation of closed cracks using subharmonic phased array. Jpn J Appl Phys 2008;47:3908. https:// doi.org/10.1143/JJAP.47.3908.

[16] Ohara Y, Potter J, Nakajima H, Tsuji T, Mihara T. Multi-mode nonlinear ultrasonic phased array for imaging closed cracks. Jpn J Appl Phys 2019;58:SGGB06. https:// doi.org/10.7567/1347-4065/ab0adc.

[17] Ohara Y, Nakajima H, Haupert S, Tsuji T, Mihara T. Imaging of three-dimensional crack open/closed distribution by nonlinear ultrasonic phased array based on fundamental wave amplitude difference. Jpn J Appl Phys 2020;59:SKKB01. https://doi.org/10.35848/1347-4065/ab79ea.

[18] Li Q, Chen Y, Tang Y, Liu H. Ultrasonic phased array detection method for butt fusion welding defects of HDPE pipes. J Phys: Conf Ser 2023;2419:012071. https:// doi.org/10.1088/1742-6596/2419/1/012071.

[19] Wu Y, Wilcox PD, Croxford AJ. Fastener hole inspection using 2D phased array. NDT E Int 2024;143:103057. https://doi.org/10.1016/j.ndteint.2024.103057.

[20] Xu N, Zhou Z. Numerical simulation and experiment for inspection of corner-shaped components using ultrasonic phased array. NDT E Int 2014;63:28–34. https://doi.org/10.1016/j.ndteint.2014.01.005.

[21] Sumana Kumar A. Phased array ultrasonic imaging using angle beam virtual source full matrix capture-total focusing method. NDT E Int 2020;116:102324. https:// doi.org/10.1016/j.ndteint.2020.102324.

[22] Hampson R, Zhang D, Gachagan A, Dobie G. Modelling and characterisation ultrasonic phased array transducers for pipe inspections. Int J Pres Ves Pip 2022; 200:104808. https://doi.org/10.1016/j.ijpvp.2022.104808.

[23] Nicolson E, Mohseni E, Lines D, Tant KMM, Pierce G, MacLeod CN. Towards an in-process ultrasonic phased array inspection method for narrow-gap welds. NDT E Int 2024;144:103074. https://doi.org/10.1016/j.ndteint.2024.103074.

[24] Dupont-Marillia F, Jahazia M, Lafreniereb S, Belangera P. Design and optimisation of a phased array transducer for ultrasonic inspection of large forged steel ingots. NDT E Int 2019;103:119–29. https://doi.org/10.1016/j.ndteint.2019.02.007.

[25] Foudzi FM, Ihara I. Development of polygonal buffer rods for ultrasonic pulse-echo measurements. J Phys: Conf Ser 2014;520:012025. https://doi.org/10.1088/1742-6596/520/1/012025.

[26] Ihara T, Tsuzuki N, Kikura H. Development of the ultrasonic buffer rod for the molten glass measurement. Prog Nucl Energy 2015;82:176–83. https://doi.org/ 10.1016/j.pnucene.2014.07.041.

[27] Kazys R, Vaskeliene V. High temperature ultrasonic transducers: a review. Sensors 2021;21:3200. https://doi.org/10.3390/s21093200.

[28] Fukuchi T, Hayashi T, Mori N. Ultrasonic focusing using a stacked thin-plate region. Jpn J Appl Phys 2023;62:SJ1005. https://doi.org/10.35848/1347-4065/ acb361.

[29] Xia M, Hayashi T, Mori N. Numerical analysis of the phased array imaging with a stacked plate buffer. Jpn J Appl Phys 2024;63:03SP55. https://doi.org/10.35848/ 1347-4065/ad25a9.

[30] Redwood M. Narrow-bandwidth pulses in solid waveguides. Mechanical waveguides. New York: Pergamon Press; 1960. p. 190–207.